Applied Physics Letters

RESEARCH ARTICLE | DECEMBER 09 2021

Submicron 3D imaging of liquid–vapor interfaces formed in the Cassie–Baxter state

S. Klingel; A. Hein ; E. Oesterschulze

Appl. Phys. Lett. 119, 231605 (2021)
https://doi.org/10.1063/5.0065934

AIP Publishing

Applied Physics Letters ARTICLE scitation.org/journal/apl

Submicron 3D imaging of liquid–vapor interfaces formed in the Cassie–Baxter state

Cite as: Appl. Phys. Lett. **119**, 231605 (2021); doi: 10.1063/5.0065934
Submitted: 6 August 2021 · Accepted: 23 November 2021 ·
Published Online: 9 December 2021

S. Klingel, A. Hein, and E. Oesterschulze[a]

AFFILIATIONS

Department of Experimental Physics, Physics and Technology of Nanostructures, University of Kaiserslautern, Erwin-Schroedinger-Str.. 46, 67663 Kaiserslautern, Germany

[a]Author to whom correspondence should be addressed: oester@physik.uni-kl.de. URL: http://www.physik.uni-kl.de/oesterschulze.

ABSTRACT

In this work, we present a method to microscopically investigate the liquid–vapor interfaces on the bottom side of droplets, which were placed on superhydrophobic structures, so that wetting in the Cassie–Baxter (CB) state occurred. These interfaces are hard to access optically, especially when an opaque substrate material is used, which is usually the case for technical applications. In that case, the menisci have to be observed through the droplet, which substantially deteriorates the imaging quality. Other methods that circumvent these distortions, such as optical coherence tomography, are restricted to a resolution of several micrometers. Confocal or fluorescence microscopy additionally requires a transparent substrate. To measure the liquid–vapor interfaces formed in the Cassie–Baxter state with high accuracy liquid droplets of a monomer solution that chemically reacts to form the elastomer, polydimethylsiloxane was placed on structured surfaces. Because double reentrant structures were used, wetting occurred in the Cassie–Baxter state despite the low surface tension of the monomer solution. After curing, it was possible to remove the solid droplets from the surface and investigate them using confocal microscopy, which provides an excellent height resolution of 10 nm. Test structures such as arrays of stripes and holes with variable spacing or diameter were used to investigate the impact of their geometry on the liquid–vapor interfaces formed in the CB state. Although the maximum height of the menisci on the droplet's bottom side is in the region of several 10 μm, the 10 nm resolution is required to adequately compare their topography with simplified theoretical models.

In the last decades, the wetting behavior of structured surfaces received a remarkable amount of attention. Especially, superhydrophobic surfaces are of great interest because of their widespread technical applications.[1–4] Most of the interesting wetting effects occur when a liquid placed on a structured surface does not impale the structure but resides on top of it; thus, the surface is only partially wetted.[5] In this so-called Cassie–Baxter state (CB state), a layer of gas partially separates the liquid from the substrate leading to a reduction of adhesive forces and high contact angles.[2]

Although wetting in the CB state is recently exploited for various technical applications, its physical principals are still on debate. Often only macroscopic properties e.g., their apparent equilibrium contact angle are studied to determine the wetting behavior of liquids on a structured surface.[6,7] They are commonly measured with an optical contact angle goniometer, where imaging is restricted to the top surface of the droplet, as outlined in black in Fig. 1(a). However, optical access to the contact area of the droplet with the structures and the CB liquid–vapor interfaces formed at its bottom side [outlined in red in Fig. 1(a)] from the top is prohibited by the strong deteriorating impact of the droplets' curvature on the imaging process. Several approaches were presented to address this issue, e.g., by using confocal or fluorescence microscopy.[8–10] These methods are, however, limited to transparent substrates because the bottom side is observed from below to avoid image distortion caused by the droplet. Additionally, they can resolve the liquid–vapor interfaces only with a height accuracy of about 1 μm.[9,10]

In this paper, we propose to place droplets of a monomer solution onto the surface of interest and polymerize the monomer to finally receive a mechanically stable polymer droplet. After its careful removal from the surface, it can be optically accessed from all sides. However, for the investigation of the wetting behavior, we have restricted imaging to the droplets' bottom side [see Fig. 1(b)] in this paper. To prove this concept, droplets of the monomer solution Dow Sylgard184 with a volume of 5 μl were placed on superhydrophobic

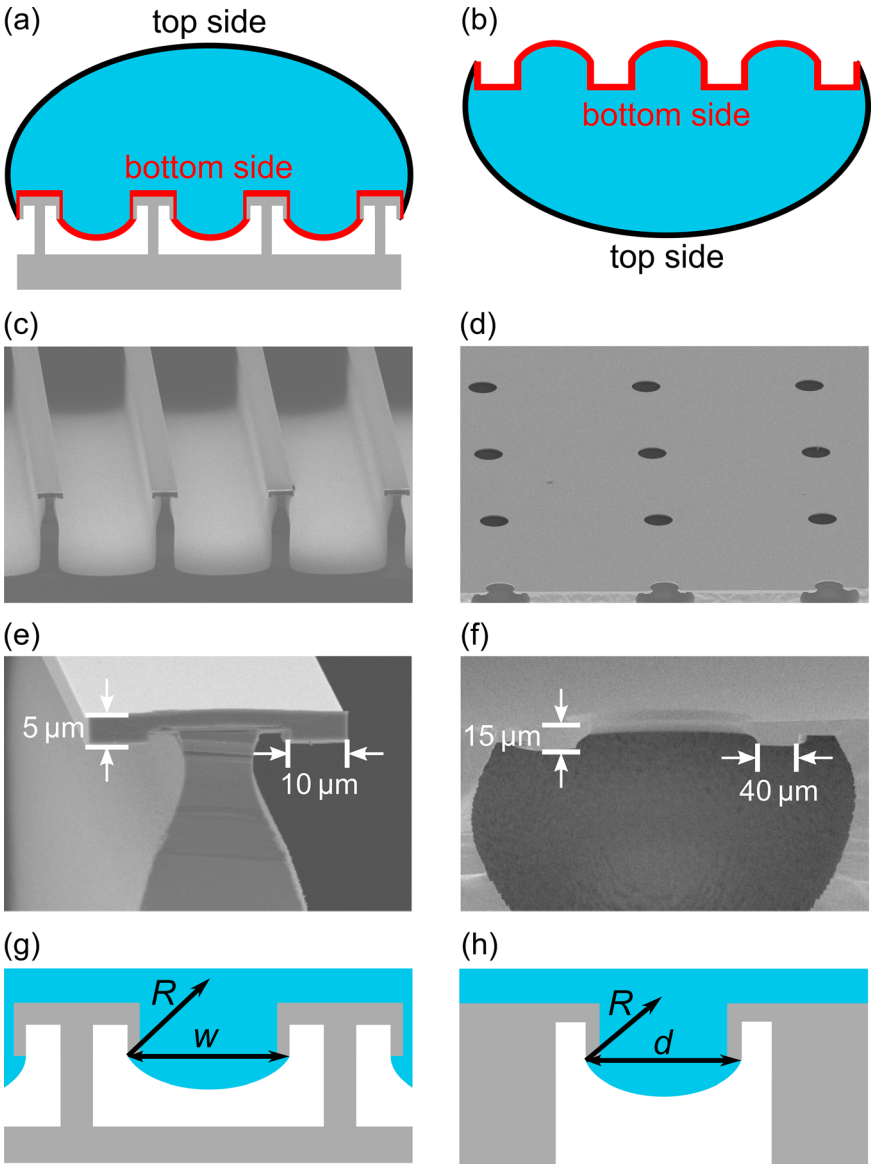

FIG. 1. (a) Droplet resting on a periodic structure. The liquid–vapor interfaces are separated in two regions: bottom side (red) and top side (black). (b) PDMS droplet after its removal from the structure. For microscopic imaging of the bottom side, the droplet is placed upside down on a sample holder. (c) and (d) SEM images of periodic stripes (stripe width 60 μm, height 110 μm, and pitch 220 μm) and holes (diameter 190 μm and pitch 1000 μm). (e) and (f) SEM images of a single stripe or hole with visible double reentrant features. (g) and (h) Sketch of the liquid–vapor interfaces formed in the CB state at the bottom side of the droplet.

double re-entrant surface structures. This geometry had to be used because it allows wetting in the CB state even for liquids with low surface tension such as the used monomer solution.[11]

Within two days at room temperature, the monomer solution cures and forms the elastomer PDMS after which the droplets can be removed from the surface. Because curing was performed at room temperature, the shrinkage of PDMS was reduced to about 0.1% and can, thus, be neglected[12] (see also the supplementary material section).

The investigated structures were periodic arrays of stripes and holes with varying spacing and diameter, respectively [see Figs. 1(c)–1(f)]. To allow for pressure compensation with the surrounding air, the holes were etched completely through the silicon substrate. The fabrication processes are described in detail in the supplementary material section.

The monomer solution was degazed in a vacuum chamber to avoid gas inclusion in the droplets, before being placed on the structured surfaces. Liquid–vapor and liquid–solid interfaces were formed in the CB state on the bottom side of the droplet, as schematically shown in Figs. 1(g) and 1(h). After curing, the solid droplets were carefully removed and placed upside down on a confocal microscope sample stage, so that the menisci spanned between the stripe structures and across the holes at the central part of the red surface shown in Fig. 1(b) are accessible for optical investigations. Those were analyzed using confocal microscopy (microsurf, NanoFocus AG, Germany) with a nominal height resolution of about 10 nm.

At first, the stripe shaped structures were examined. Figure 2(a) shows the central section of the bottom side of a cured PDMS droplet that was removed from an array of stripes with a spacing of

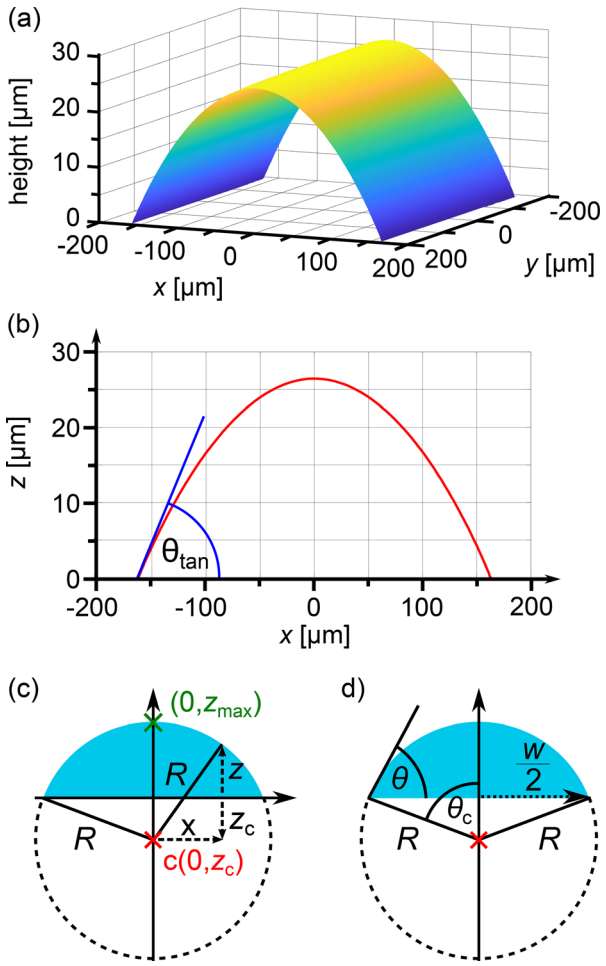

FIG. 2. (a) Confocal microscope image of a liquid–vapor interface between two adjacent stripes ($w = 330\ \mu$m). (b) 2D section of the same liquid–vapor interface along the x-axis at $y = 0$. The blue tangent shows the inclination near $z = 0$, which was evaluated to obtain the contact angle $\theta = 18.8°$ between the CB liquid–vapor interfaces and the stripes directly from the measured data. (c) Sketch of a circular segment used to describe a single feature of the CB liquid–vapor interface. $c(0, z_c)$ marks the center of the cylinder. The light blue cap represents the measured surface shown in (a). (d) Illustration for the calculation of the contact angle θ of a liquid–vapor interface.

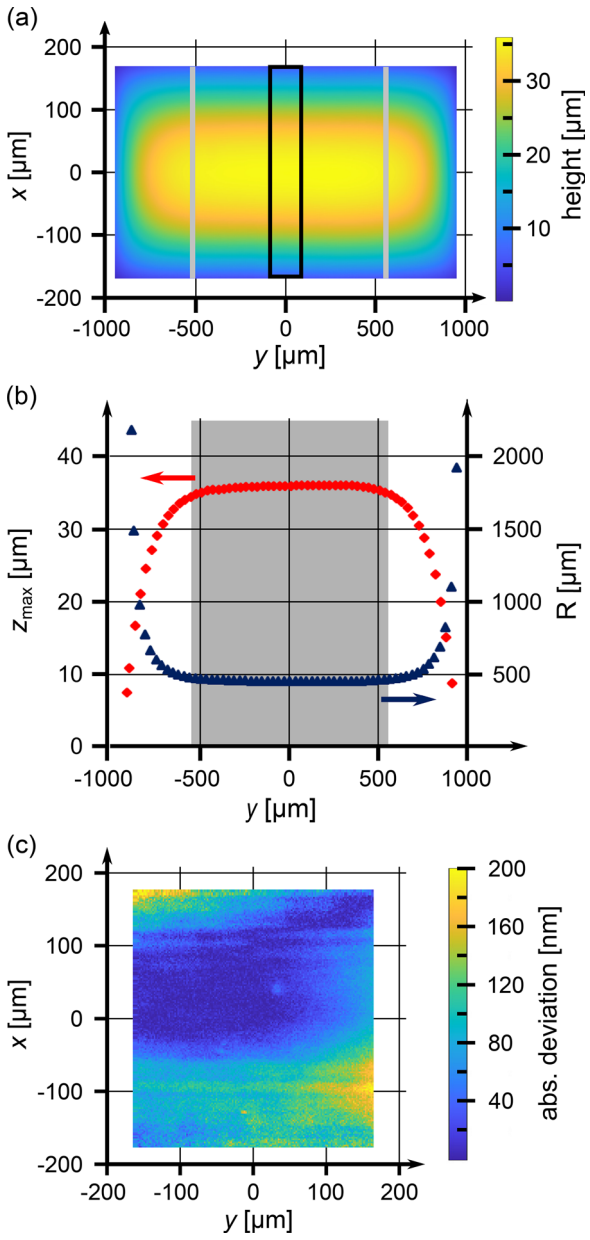

FIG. 3. (a) Confocal microscopy image of a complete CB liquid–vapor interface spanned between two adjacent stripes ($w = 355\ \mu$m). (b) Maximum height (red diamonds) and radius (blue triangles) of 2D sections along the x-axis in relation to the location along the y-axis. In the gray area, the deviation between $z_{max}(y)$ and $\max(z_{max}(y))$ as well as $R(y)$ and $\min(R(y))$ is less than 2%. This area is identical to that found between the gray vertical lines in (a). (c) Colormap of the absolute deviation between the fitted cylindrical model and the measured height of the liquid–vapor interface for the black rectangle in (a).

$w = 330\ \mu$m (an image of the complete bottom side of a droplet can be found in the supplementary material section).

Because of the symmetry of the stripes, a cylindrical model was used to describe the central part of the shape of the CB liquid–vapor interfaces. This means that cross sections perpendicular to the stripes along the x-axis [see Fig. 2(b)] were assumed to be circular segments with height z_{max}, base diameter w, radius R, and central angle θ_c, as seen in Figs. 2(c) and 2(d).

In this model, the height-distribution $z(x)$ is assumed to be independent from y. As exemplary shown for another stripe structure with $w = 355\ \mu$m in Fig. 3(a), this holds true for the area near the center of the CB liquid–vapor interface. However, at the left and right caps close to the droplet's edge, the CB liquid–vapor interface starts to become more complex and cannot be described as a simple cylinder anymore. To identify when these deviations become apparent, 2D sections were measured on varying locations along the y-axis. Then, z_{max} and R were determined for each cross section and plotted in

relation to y [see Fig. 3(b)]. In the region $y = -430$ to $y = 470$ μm (gray background), the deviation of $z_{max}(y)$ compared to $\max(z_{max}(y)) = 36.1$ μm and of $R(y)$ compared to $\min(R(y)) = 462.1$ μm is lower than 2%; thus, the 2D sections are nearly independent from y. The areas that are theoretically examined in this paper are located in this region; thus, the cylindrical model is adequate.

The equation for a circular segment with $z(x = 0) = z_{max}$ is given by

$$R^2 = x^2 + (z - z_c)^2 \iff z = z_c + \sqrt{R^2 - x^2}. \tag{1}$$

Note that z_c is negative for $\theta_c < 90°$. The maximum height can be calculated as

$$z_{max} = z(x = 0) = R + z_c \iff R = z_{max} - z_c. \tag{2}$$

Inserting Eq. (2) in Eq. (1) leads to

$$z = z_c + \sqrt{(z_{max} - z_c)^2 - x^2}. \tag{3}$$

Equation (3) was fitted to the measured data to receive z_c and z_{max}, necessary to calculate R with Eq. (2).

With the two parameters z_{max} and R, it is then also possible to calculate the contact angle θ at the base of the CB liquid–vapor interface, which is equal to the central angle θ_c of the circular segment. However, these angles deviate from each other at the caps left and right of the cylindrical structure, that is outside of the gray area shown in Figs. 3(a) and 3(b). From Figs. 2(c) and 2(d), the following equation can be derived:

$$\begin{aligned} \cos(\theta) &= -\frac{z_c}{R} = -\frac{z_{max} - R}{R}, \\ \iff \theta &= \arccos\left(1 - \frac{z_{max}}{R}\right). \end{aligned} \tag{4}$$

Without any forces acting on the liquid–vapor interfaces, the contact angle received from Eq. (4) should be nearly 0° because of the low surface tension $\sigma_{lv} = 20.4$mN/m of PDMS.[13]

There exists, however, a pressure difference ΔP_{YL} across the droplet's surface caused by its curvature, which can be calculated by the Young–Laplace equation:

$$\Delta P_{YL} = \sigma_{lv}\left(\frac{1}{R_1} + \frac{1}{R_2}\right). \tag{5}$$

When the droplets are placed on stripe shaped surfaces, they show an elongated shape because pinning occurs solely perpendicular to the stripes' direction.[15] This leads to two distinct macroscopic radii of curvatures $R_\perp$ and $R_{||}$, which are measured by imaging the droplets' top side in both directions with an optical contact angle goniometer and then fitting ellipses to its shape (see Fig. 4). The elliptic shapes are caused by the additional gravitation force acting on the droplet.[14] The radii of curvature for both directions were calculated for the co-vertex that is marked with a blue cross in Fig. 4 using the length of the semi-axes.

The height h of the droplet additionally leads to a hydrostatic pressure at the CB liquid–vapor interfaces, which is given as $\Delta P_h = \rho g h$ with the density ρ of PDMS. This leads to a total pressure drop of $\Delta P = \Delta P_{YL} + \Delta P_h$. By applying the Young–Laplace equation to the liquid–vapor interfaces between the stripes and using the radius R given by the cylindrical model, the pressure drop ΔP^* on the bottom side can also be calculated as

$$\Delta P^* = \frac{\sigma_{lv}}{R}, \tag{6}$$

because the second radius of curvature for a cylinder is given as $R_2 = \infty$.

At first, the absolute deviation between the measured surface outlined with a black rectangle in Fig. 3(a) and the one obtained from fitting Eq. (3) to the so received data is shown in Fig. 3(c). The coefficient of determination for the excellent fit exceeds 0.999, and the found parameters were $z_c = -426.0$ μm and $z_{max} = 36.1$ μm.

The overall deviation is below 200 nm, and in most areas even lower than 100 nm. The deviations are presumably caused by a slight tilt of the sample or imperfections of the stripes. They are, however, low enough to conclude that the cylindrical model is adequate to describe the liquid–vapor interfaces between stripes near the center of a droplet.

To further prove the quality of the cylindrical model, the contact angle was also evaluated with a second method: The inclination angle near $z = 0$ of a 2D section along the x-axis should match the contact angle as seen in Fig. 2(b). This way the contact angle θ_{tan} could be

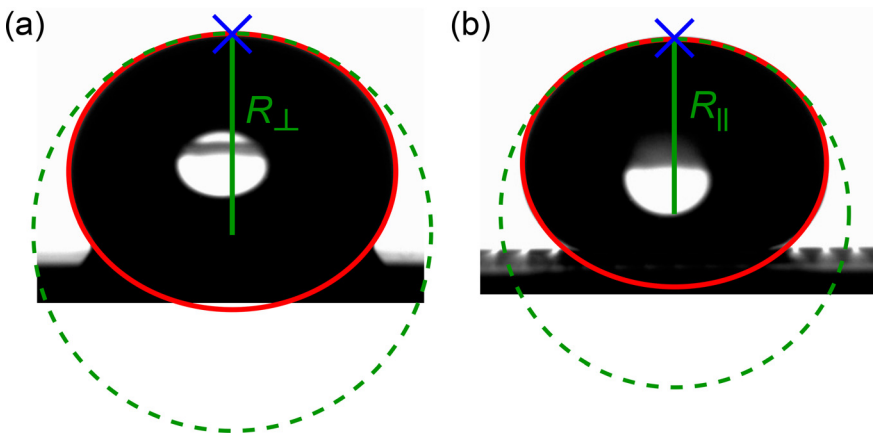

FIG. 4. Optical images of a PDMS droplet on a stripe structure: (a) recorded perpendicular and (b) parallel to the stripes. The red ellipses are the best approximation for the shape of the droplet's edge in these directions. The green dashed circles have the same radius ($R_\perp = 1578$ μm and $R_{||} = 1394$ μm) as the ellipse in the co-vertex marked with a blue cross.

TABLE I. Fit parameters for the cylindrical model applied to the measured CB liquid–vapor interfaces. Additionally, the contact angles given by the model and directly evaluated from the height data and the macro- and microscopically determined pressure drops are given. The accuracy of the distance between adjacent stripes is given as $\Delta w = \pm 1\,\mu$m.

w (μm)	z_{max} (μm)	z_c (μm)	R (μm)	θ (°)	θ_{tan} (°)	ΔP_{YL} (Pa)	ΔP_h (Pa)	ΔP (Pa)	ΔP^* (Pa)
220	13.0	−450.4	463.4	13.6	13.9	26.6	16.6	43.2	43.2
330	27.5	−490.1	517.6	18.8	18.9	20.7	18.4	39.1	38.6
355	36.1	−426.0	462.1	22.8	23.3	26.8	15.7	42.5	43.3
390	47.8	−424.2	472.0	26.0	26.2	26.0	16.2	42.2	42.4
470	57.9	−435.8	493.7	28.0	28.3	22.2	17.5	40.5	39.7
510	72.0	−419.2	491.2	31.4	31.8	22.9	16.9	39.8	40.7

evaluated directly using the height data and then be compared with θ found from the model. Table I summarizes all the parameters addressed in the previous sections.

The pressure drop is approximately 40 Pa for all structures, and the difference between ΔP and ΔP^* is always lower than 1 Pa, indicating good agreement between the macroscopically (top side) and microscopically (bottom side) measured liquid–vapor interfaces. Because the pressure applied on them is similar for all geometries, the radii of the cylinders are also similar. Therefore, the height of the liquid–vapor interfaces should grow approximately quadratic with increasing distance between the stripes, which follows from calculating z_{max} as a function of R and w and subsequently using its first order series approximation,

$$z_{max} = R - \frac{1}{2}\sqrt{4R^2 - w^2} \approx \frac{w^2}{8R} \quad \text{for} \quad w < R. \tag{7}$$

This behavior can clearly be seen in Table I. It should also be noted that θ and θ_{tan} deviate less than 0.5° from each other, underlining the model's validity.

In the second part, arrays of holes are investigated, and the results compared to those found for stripes. Figure 5(a) shows the CB liquid–vapor interface, which was spanned over a single hole with a diameter of $d = 490\,\mu$m. Because of the rotational symmetry, a spherical cap with radius R_{sph} and base diameter d was used as a fit function for the meniscus.

Similar to the stripes, it can be expected that the liquid–vapor interface near the perimeter of the droplet cannot be described with this model. However, as seen in Fig. 5(b) for an array of holes with $d = 190\,\mu$m, only the interfaces in direct vicinity to the perimeter are distorted. All others have an identical shape; thus, the investigation of a single hole is sufficient to describe nearly the complete bottom side of the droplet.

The origins of the chosen single droplet x- and y-axis were placed in the center of the liquid–vapor interface, so that the equation of the sphere can be written as

$$R_{sph}^2 = x^2 + y^2 + (z - z_c)^2. \tag{8}$$

The height distribution $z(x, y)$ of the liquid–vapor interface is then given by

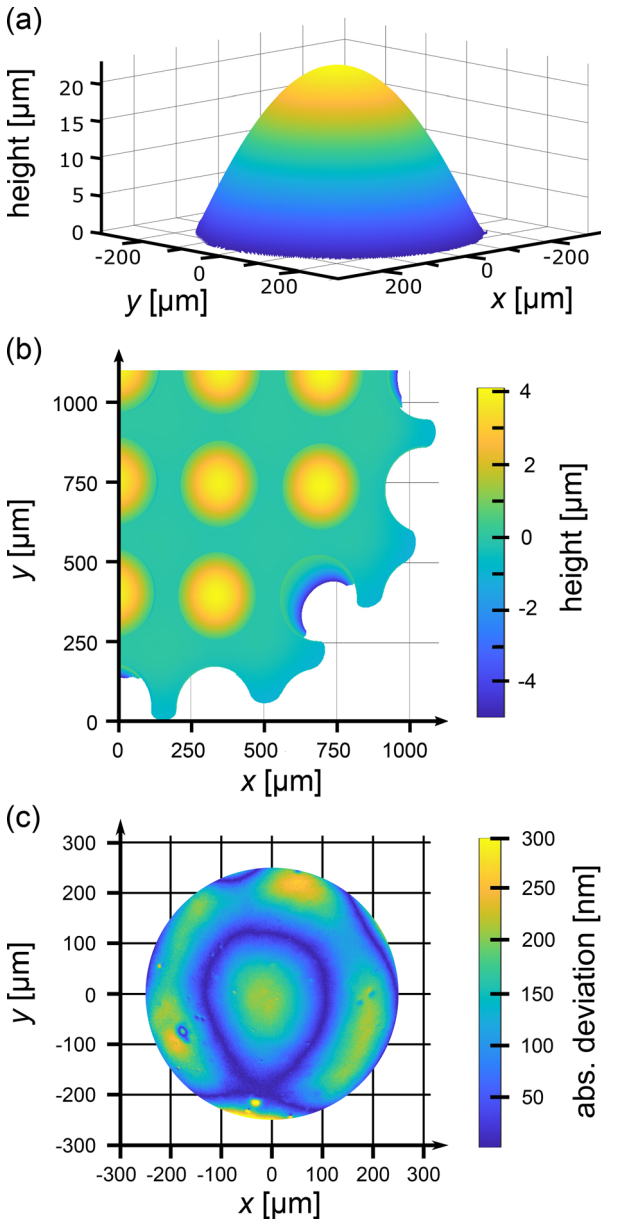

FIG. 5. (a) Confocal microscope image of the CB liquid–vapor interface spanned over a single hole ($d = 490\,\mu$m). (b) Confocal microscope image of the bottom side of a droplet, which was cured on an array of holes with $d = 190\,\mu$m. The image shows a section near the droplet's perimeter. (c) Colormap of the absolute deviation between the fitted spherical model and the measured height of the liquid–vapor interface shown in (a).

$$z = z_c + \sqrt{R_{sph}^2 - x^2 - y^2}. \tag{9}$$

This model can also be illustrated by Figs. 2(b) and 2(c) when w is replaced by d. Because the z-axis originates at the base of the cap, the radius of the sphere can be expressed as $R_{sph} = z_{max} - z_c$. Inserting this relation in Eq. (9) leads to the following expression:

$$z = z_c + \sqrt{(z_{max} - z_c)^2 - x^2 - y^2}, \quad (10)$$

which was used to fit the measured data. The equation for the contact angle is the same as for the cylindrical surfaces [see Eq. (4)].

Macroscopic images of the droplet's top side are again used to determine the pressure acting on the liquid–vapor interfaces, but this time, the structures are isotropic, so that only one radius of curvature R_{top} exists. Because gravity still acts on the droplet, it also has an elliptic shape, and R_{top} has to be calculated as before. The pressure drop caused by the curvature of the droplet is then given by

$$\Delta P_{YL} = \frac{2\sigma_{lv}}{R_{top}}. \quad (11)$$

Again ΔP_h has to be added to ΔP_{YL} to obtain the total pressure acting on the liquid–vapor interfaces on the bottom side.

Because of the spherical shape of the liquid–vapor interfaces spanned over the holes, the pressure drop given by the microscopic data is calculated as

$$\Delta P^* = \frac{2\sigma_{lv}}{R_{sph}}. \quad (12)$$

The absolute deviation between the spherical model and the measured CB liquid–vapor interface spanned over a hole with $d = 490\ \mu$m is shown in Fig. 5(c). The coefficient of determination exceeds 0.999, and the evaluated parameters for the sphere are $z_c = -1237.7\ \mu$m and $z_{max} = 23.3\ \mu$m.

The deviation reaches a maximum of 300 nm, which is slightly higher compared to that of the stripes. This is presumably caused by the not perfectly circular shape of the holes received by the fabrication process. Due to excessive etching needed to open the holes through the silicon wafer, the structures may be slightly distorted. Still, the spherical model describes the meniscus with acceptable accuracy below the sub-micrometer range.

Once again, the contact angle θ_{tan} was evaluated using a 2D section. Table II comprises the parameters found for the spherical model.

The results are similar to those found for periodic stripes. Again θ_{tan} does not deviate from θ by more than 0.5°, and ΔP is nearly equal to ΔP^* for all structures.

Also, z_{max} and θ are increasing with the diameter of the holes but are generally lower for those structures compared to stripes with $w = d$. This behavior is expected when Eqs. (6) and (12) are compared. The radius R_{sph} for spherical surfaces is twice as high compared to R for cylindrical ones if the same pressure is applied. This, in turn, leads to a lower z_{max} [see Eq. (7)]. Additionally, the pressure drop in Table II is about 25% lower compared to those in Table I for all structures, which is a result of lower macroscopic contact angles for the droplets on hole structures. This leads to a factor of roughly 2.5 between R_{sph} and R.

TABLE II. Parameters for a spherical model applied to the measured liquid–vapor interfaces spanned over holes with various diameters. The deviation of the diameter of the holes is given as $\Delta d = \pm 2.5\ \mu$m.

d (μm)	z_{max} (μm)	z_c (μm)	R_{sph} (μm)	θ (°)	θ_{tan} (°)	ΔP_{YL} (Pa)	ΔP_h (Pa)	ΔP (Pa)	ΔP^* (Pa)
190	3.7	−1358.9	1362.6	4.2	3.7	16.8	11.7	28.5	29.4
390	13.5	−1396.5	1410.0	8.0	7.5	17.1	11.6	28.7	28.4
490	23.3	−1237.7	1261.0	11.0	10.6	17.9	14.5	32.4	31.7
600	37.6	−1187.0	1224.6	14.2	13.8	17.6	14.6	32.2	32.6

This can be of interest when superhydrophobic structures, which should provide a stable wetting in the CB state even when a high pressure is applied, are designed. In this case, the stability of the CB state can be affected negatively by the curvature of the liquid–vapor interfaces between the structures, for example, when the liquid touches the substrate caused by the sagging or when the contact angle between the CB liquid–vapor interfaces and the stripes or holes reaches the advancing contact angle of the material, so that the droplet can even wet double re-entrant structures.

In conclusion, this work provides a way to investigate CB liquid–vapor interfaces of a cured PDMS droplet released from a double re-entrant structure. It, thus, serves as a snapshot of the current wetting state. After its removal, the droplet is optically accessible from all directions. However, we imaged solely the droplets' bottom side to investigate their wetting behavior. Because of its excellent resolution and the ability to directly receive topographic information of the droplet, confocal microscopy was proven to be suited for this task. Simplified models were introduced to describe the meniscis' geometry near the center of the droplet in good agreement with the measured height data. We found that depending on the geometry, significant sagging occurs even for a total pressure of only 40 Pa or less. In particular, the stripe structures are prone to this effect, which needs to be considered for technical applications.

See the supplementary material for:

- The fabrication process for double re-entrant structures.
- An example of a confocal microscopy image of a large area at the bottom side of the droplet obtained from a stripe structure.
- The investigation of the shrinkage of a PDMS droplet during its curing process at room temperature.

We wish to thank Professor Dr. J. Seewig (Institute for Measurement and Sensor Technology, University of Kaiserslauten, Germany) for supporting us with the confocal microscope.

AUTHOR DECLARATIONS

Conflict of Interest

The authors have no conflicts to disclose.

DATA AVAILABILITY

The data that support the findings of this study are available from the corresponding author upon reasonable request.

REFERENCES

[1]M. Ferrari, A. Benedetti, E. Santini, F. Ravera, L. Liggieri, E. Guzman, and F. Cirisano, Colloids Surf., A **480**, 369 (2015).
[2]G. D. Bixler and B. Bhushan, Philos. Trans. R. Soc., A **370**, 2381 (2012).
[3]J. Brennan, D. Fairhurst, R. Morris, G. McHale, and M. Newton, J. Phys. D: Appl. Phys. **47**, 205302 (2014).
[4]J. C. Brennan, N. R. Geraldi, R. H. Morris, D. J. Fairhurst, G. McHale, and M. I. Newton, Sci. Rep. **5**, 10267 (2015).
[5]A. B. D. Cassie and S. Baxter, Trans. Faraday Soc. **40**, 546 (1944).
[6]T. Omori and T. Kajishima, Phys. Fluids **29**, 112107 (2017).

[7]H. Y. Erbil, Colloids Interfaces **5**, 8 (2021).
[8]P. Papadopoulos, X. Deng, L. Mammen, D.-M. Drotlef, G. Battagliarin, C. Li, K. Müllen, K. Landfester, A. del Campo, H.-J. Butt, and D. Vollmer, Langmuir **28**, 8392 (2012).
[9]F. Schellenberger, N. Encinas, D. Vollmer, and H.-J. Butt, Phys. Rev. Lett. **116**, 096101 (2016).
[10]P. Lv, Y. Xue, Y. Shi, H. Lin, and H. Duan, Phys. Rev. Lett. **112**, 196101 (2014).
[11]T. Liu and C.-J. Kim, Science **346**, 1096 (2014).
[12]M. H. Madsen, N. A. Feidenhans'l, P.-E. Hansen, J. Garnæs, and K. Dirscherl, J. Micromech. Microeng. **24**, 127002 (2014).
[13]S. Gohil, S. Suhail, J. Rose, T. Vella, and L. Nair, "Chapter 8—Polymers and composites for orthopedic applications," in *Materials for Bone Disorders*, edited by S. Bose and A. Bandyopadhyay (Academic Press, 2017), p. 349.
[14]V. A. Lubarda and K. A. Talke, Langmuir **27**, 10705 (2011).
[15]W. Choi, A. Tuteja, J. M. Mabry, R. E. Cohen, and G. H. McKinley, J. Colloid Interface Sci. **339**, 208 (2009).